

## Article

# Stoichiometry Dependence of Physical and Electrochemical Properties of the SnO<sub>x</sub> Film Anodes Deposited by Pulse DC Magnetron Sputtering

Yibo Ma, Xiaofeng Zhang, Weiming Liu, Youxiu Wei, Ziyi Fu, Jiuyong Li, Xuan Zhang, Jingjing Peng and Yue Yan \*

Beijing Engineering Research Center of Advanced Structural Transparencies for the Modern Traffic System, Beijing Institute of Aeronautical Materials, Beijing 100095, China; mayibo555@163.com (Y.M.); xiaofeng.zhang@biam.ac.cn (X.Z.); avic\_weiming@126.com (W.L.); qiulinhaizai@163.com (Y.W.); fu19801297313@163.com (Z.F.); 15737936609@163.com (J.L.); kaixuan1226@163.com (X.Z.); pij.csu.mat@163.com (J.P.)

\* Correspondence: yue.yan@biam.ac.cn; Tel.: +86-(010)-6249-6499

**Abstract:** A batch of Sn oxides was fabricated by pulse direct current reactive magnetron sputtering (pDC–RMS) using different Ar/O<sub>2</sub> flow ratios at 0.3 Pa; the influence of stoichiometry on the physical and electrochemical properties of the films was evaluated by the characterization of scanning electron microscope (SEM), X-ray diffraction (XRD), X-ray reflection (XRR), X-ray photoelectron spectroscopy (XPS) and more. The results were as follows. First, the film surface transitioned from a particle morphology (roughness of 50.0 nm) to a smooth state (roughness of 3.7 nm) when Ar/O<sub>2</sub> flow ratios changed from 30/0 to 23/7; second, all SnO<sub>x</sub> films were in an amorphous state, some samples deposited with low O<sub>2</sub> flow ratios ( $\leq 2$  sccm) still included metallic Sn grains. Therefore, the stoichiometry of SnO<sub>x</sub> calculated by XPS spectra increased linearly from SnO<sub>0.08</sub> to SnO<sub>1.71</sub> as the O<sub>2</sub> flow ratios increased, and the oxidation degree was further calibrated by the average valence method and SnO<sub>2</sub> standard material. Finally, the electrochemical performance was confirmed to be improved with the increase in oxidation degree (x) in SnO<sub>x</sub>, and the SnO<sub>1.71</sub> film deposited with Ar/O<sub>2</sub> = 23/7 possessed the best cycle performance, reversible capacity of 396.1 mAh/g and a capacity retention ratio of 75.4% after 50 cycles at a constant current density of 44  $\mu$ A/cm<sup>2</sup>.

**Keywords:** tin oxide film; reactive magnetron sputtering; oxygen vacancy; cycle performance



**Citation:** Ma, Y.; Zhang, X.; Liu, W.; Wei, Y.; Fu, Z.; Li, J.; Zhang, X.; Peng, J.; Yan, Y. Stoichiometry Dependence of Physical and Electrochemical Properties of the SnO<sub>x</sub> Film Anodes Deposited by Pulse DC Magnetron Sputtering. *Materials* **2021**, *14*, 1803. <https://doi.org/10.3390/ma14071803>

Academic Editor:  
Annett Dörner-Reisel

Received: 20 February 2021  
Accepted: 27 March 2021  
Published: 6 April 2021

**Publisher's Note:** MDPI stays neutral with regard to jurisdictional claims in published maps and institutional affiliations.



**Copyright:** © 2021 by the authors. Licensee MDPI, Basel, Switzerland. This article is an open access article distributed under the terms and conditions of the Creative Commons Attribution (CC BY) license (<https://creativecommons.org/licenses/by/4.0/>).

## 1. Introduction

Tin oxide (SnO<sub>x</sub>) has been applied as a promising anode since the Fuji Co. first proposed the use of SnO<sub>x</sub> in lithium-ion batteries [1,2]. Although SnO<sub>x</sub> possesses better cycle performance than the pure Sn electrode [3], it still suffers the problems of irreversible capacity loss and rapid capacity decay arising from the mechanical failure (e.g., cracking, pulverization and disconnection) during discharge/charge cycles [4,5]. It is known that SnO<sub>x</sub> would transform into “Li<sub>2</sub>O matrix and metallic Sn” and would be surrounded by solid electrolyte interphase (SEI) during the first lithiation process; Li<sub>2</sub>O could prevent Sn nanoparticles from congesting into large clusters and partially alleviate large volume strain [6]; however, the Li<sub>2</sub>O and SEI layers are not effective electronic conductors and could not store Li<sup>+</sup> reversibly; both of them would result in increased impedance and irreversible capacity loss [7,8]. In addition, different nanosized SnO<sub>x</sub> (nanoparticles [9], nanorods [10], nanofibers [11] and nanofilms [12–14]) have been devoted to relieving the mechanical failure and providing much shorter Li<sup>+</sup> transfer paths to improve cycle performance [15]; on the contrary, the increased specific surface area would increase the electrode impedance and exhibit a greater irreversible capacity loss. Therefore, there is a special stoichiometry SnO<sub>x</sub> corresponding to the best cycle performance.

SnO<sub>x</sub> nanofilm is one kind of anode used in thin film lithium-ion batteries and can be fabricated by many methods, such as chemical vapor deposition (CVD) [16], radio

frequency magnetron sputtering (RF–MS) [14], molecular beam epitaxial (MBE) [17], pulse laser deposition (PLD) [18] and spray pyrolysis (SP) [19,20]. Among these methods, MS has been proven to be an ideal approach for preparing films, since it is simple, manageable and convenient to control the film thickness, composition and structure [21,22]. In addition, reactive magnetron sputtering (RMS, sputtering with introduced reactive gas) could prepare special film composition different from the target, and even control the film composition precisely by adjusting the partial pressure of reactive gas. However, the sputtering mode would lie in a spontaneous conversion between the metal and oxide deposition mode when the oxygen partial pressure increases gradually [23]; then, a transition state in film composition is formed. For instance, the SnO<sub>2</sub> films prepared by RF–RMS have good cycle performance and show a stable capacity of 440 μAh/cm<sup>2</sup>·μm after 100 cycles at a constant current density of 300 μA/cm<sup>2</sup> in the range of 0.1–1.0 V [9]. Furthermore, the Ar/O<sub>2</sub> flow ratio is a key factor determining the oxidation degree of SnO<sub>x</sub> when conducting the deposition at a fixed working pressure; a set of SnO<sub>x</sub> films with increasing x values have been fabricated by tuning the Ar/O<sub>2</sub> flow ratios [11]; it could be inferred that the structural and optical properties dramatically depend on the deviation of composition [20]. However, there is no systematic research illustrating the influence of oxidation degree on electrochemical performance and introducing a gradual evolution when the SnO<sub>x</sub> composition transforms from a low oxygen ratio to a high oxygen ratio.

In this paper, a group of SnO<sub>x</sub> films was prepared via pDC–RMS using different Ar/O<sub>2</sub> flow ratios, and then, all properties, such as morphology, microstructure, surface chemistry and electrochemical properties, were evaluated and compared with each other. Later, a special stoichiometry SnO<sub>x</sub> was obtained corresponding to the best cycle performance. This work helps us to obtain a better understanding of the O:Sn atomic ratio effect on comprehensive performance.

## 2. Experimental Analysis

The SnO<sub>x</sub> films were directly deposited on two types of substrates, Cu foils (Dilo Corporation, Dongguan, China, 30 μm thickness, 99.3% purity) and glass sheets (Schoot Corporation, Suzhou, China, sodalime–silicate glass, 1.0 mm thickness). The deposition process was carried out under the following conditions: pure Sn target (Dream Material Technology Corporation, Beijing, China, 99.99% purity, Φ75 × 4 mm) was selected; the target–substrate distance, sputtering pressure, substrate temperature and the sputtering power were fixed at 18 cm, 0.3 Pa, 25 °C and (0.45 W/cm<sup>2</sup>, 100 kHz, 70% of duty cycle), respectively. Then, the SnO<sub>x</sub> films with different Ar/O<sub>2</sub> flow ratios (30/0, 29/1, 28/2, 26/4, 25/5, 24/6, 23/7) were fabricated one by one. Other SnO<sub>x</sub> films with approximate thicknesses of ≈130 μm were prepared later with the aid of deposition rate, as shown in Figure 1b, and these films were then used to characterize transmittance, roughness and other properties.

The physical properties of the deposited films were characterized as follows. First, field emission scanning electron microscopy (FESEM, SU-8010, Hitachi, Tokyo, Japan) and an atomic force microscope (AFM, Dimension Edge, Bruker, Karlsruhe, Germany) were used to measure the film thickness, morphology and roughness; both the surface and cross–section SEM images were taken by operating under vacuum at a voltage of 30 kV, whereas the AFM images were detected in atmosphere with tapping mode. As for the morphology of the cycled electrodes, the half-cells were dismantled in a glove box and were rinsed in acetone to eliminate residual salts, and then, the examination was performed. Second, the crystal structure and film density were analyzed by X-ray diffraction (XRD, D8 Advance, Bruker, Karlsruhe, Germany) and X-ray reflection (XRR) methods, individually; both of them were measured with the same equipment and X-rays sources (Cu Kα, λ = 0.15418 nm, voltage of 40 kV, current of 40 mA), but with different scanning ranges (10°–80° for XRD; 0°–3° for XRR) and analytical methods. Third, X-ray photoelectron spectroscopy (XPS, Quantera SXM, PHI, Chigasaki, Japan) was conducted by using focused monochromatized Al Kα radiation (1486.6 eV) with a beam size of

$\approx 200 \mu\text{m}^2$  at an incident angle of  $45^\circ$ . All the reported binding energy data were calibrated using the position of the carbon contamination (284.8 eV) on the surface of  $\text{SnO}_x$  films. Then, the analysis of XPS data was performed, and the peak deconvolutions were realized by applying the sum of “70% Gaussian–30% Lorentzian” line shapes after Shirley-type background subtraction; the results were also calibrated by the spectra with  $\text{Ar}^+$  etching and the  $\text{SnO}_2$  power standard material ( $\text{SnO}_2$ ,  $M = 150.71$ , CAS:18282–10–5, AR 99.5%, Aladdin Co., Shanghai, China). An additional valence band (VB) spectrum was further measured by XPS using the same  $\text{Al K}\alpha$  radiation to reveal oxidation state. Lastly, the optical properties were performed in the wavelength range of 300–800 nm by a UV–Visible spectrometer (Cary 5000, Varian, Palo Alto, CA, USA).

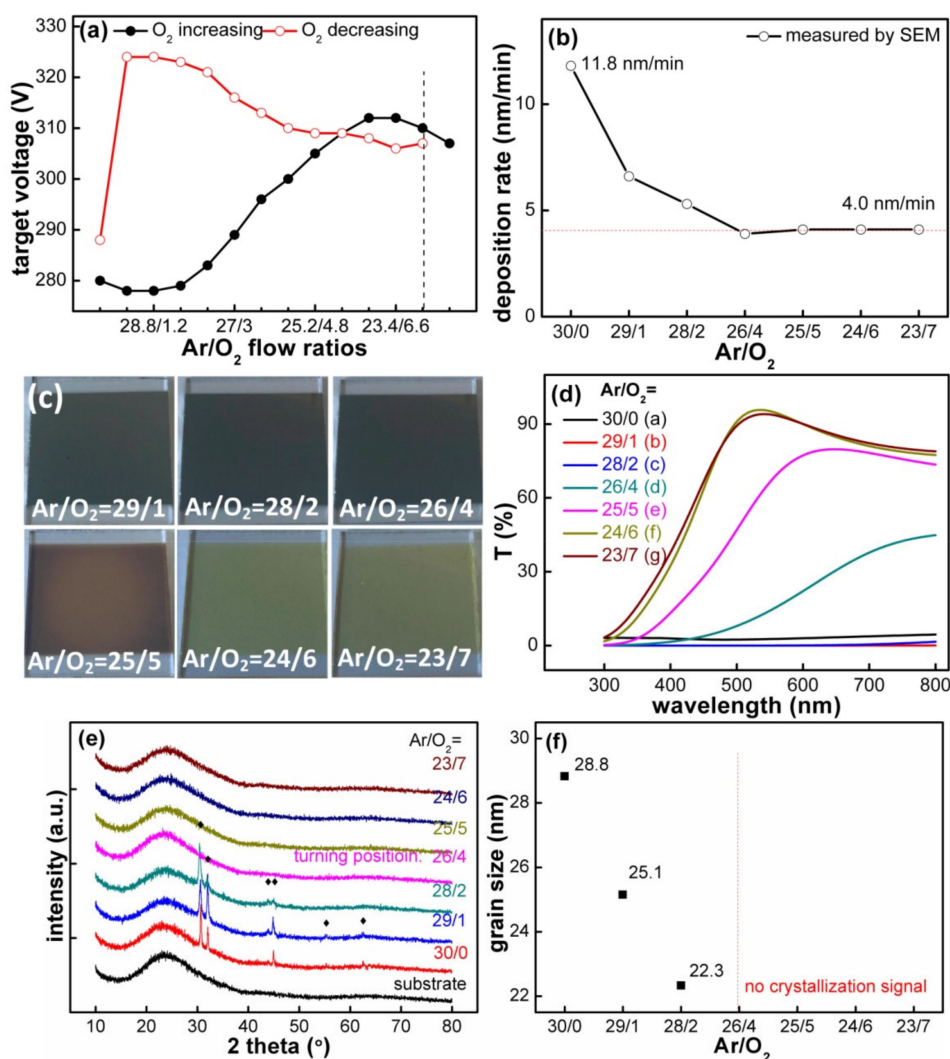


**Figure 1.** (a) Voltage hysteresis curve, (b) deposition rate, (c) optical images, (d) transmittance curves, (e) XRD patterns and (f) average grain size of the  $\text{SnO}_x$  films deposited with various  $\text{Ar}/\text{O}_2$  flow ratios.

Standard two-electrode (CR 2025) coin cells were assembled with  $\text{SnO}_x$  film on Cu foil as the working electrode, metallic lithium foil as the counter and reference electrodes and the microporous polyethylene film (PE, 30  $\mu\text{m}$  in thickness, Linyi Gelon New Battery Material Co., Linyi, China) as the separator; hence, the half-cell was set as a configuration of Li metal (–) | separator |  $\text{SnO}_x$  (+). Then, the coin cell was immersed in liquid electrolyte, 1.0 mol/L  $\text{LiPF}_6$  in a mixture of ethylene carbonate (EC), dimethyl carbonate (DMC) and ethyl methyl carbonate (EMC), with the volume ratio of 1:1:1. All coin cells were assembled in a glove box with moisture and oxygen contents of less than 1 ppm. Galvanostatic

charge/discharge was carried out using a constant current of  $44 \mu\text{A}/\text{cm}^2$  between 0.01 and 1.2 V with a battery tester (CT2001A, LAND, Wuhan, China), and the rate performance was performed in the mutative current density range ( $22\text{--}176 \mu\text{A}/\text{cm}^2$ ). CV curves were measured using an electrochemical workstation (650e, CHI, Shanghai, China), with a scanning rate of 0.1 mV/s between 0.01 and 2.0 V; electrochemical impedance spectroscopy (EIS) was then performed with a voltage amplitude of 5 mV in the frequency range of  $10^{-2}\text{--}10^6$  Hz.

### 3. Results and Discussion

#### 3.1. Basic Physical Properties of the $\text{SnO}_x$ Films

It is known that MS is a technique for the preparation of thin film based on gas discharge; the partial pressure of introduced oxygen is critical to the sputtering state when performing RMS from the metallic target [24]. Hence, we first investigated the target voltage as a function of Ar/O<sub>2</sub> flow ratios at a fixed working pressure, as shown in Figure 1a. The target voltage hysteresis curve of SnO<sub>x</sub> film was different from that of the SiO<sub>2</sub> film deposited with the same Ar/O<sub>2</sub> atmosphere and the pure Si target. The Sn target voltage increased by 30 V abruptly and reached a maximum voltage when O<sub>2</sub> flow ratios increased from 1.8 to 6.0 sccm; then, it gradually decreased to a voltage of 305 V as the O<sub>2</sub> flow ratios increased from 6.0 to 7.0 sccm; severe fluctuation did not occur until the O<sub>2</sub> flow ratio exceeded 7.4 sccm. With the following decrease in O<sub>2</sub> flow ratios, the target voltage showed a hysteresis in the region between 7 and 0.6 sccm, and finally, the target voltage returned to 288 V; the reason for this is that Ar gas has higher sputtering efficiency than O<sub>2</sub>, and the higher the Ar flow ratio is, the greater sputtering yield is. Therefore, the detected hysteresis curve determined a reasonable sputtering atmosphere (O<sub>2</sub> flow ratio was less than 7 sccm), which prevented the Sn target from poisoning and maintained a continuous deposition. With the selected Ar/O<sub>2</sub> flow ratios, the deposition rates shown in Figure 1b were calculated by the film thickness measured from the cross-section images (in Figure S1). It could also be seen that the films deposited quickly when performing with low O<sub>2</sub> flow ratios (O<sub>2</sub> ≤ 2 sccm) because of the metal deposition mode, and they gradually attenuated to a stable value of 4.0 nm/min with the increase in O<sub>2</sub> flow ratios; one turning point (Ar/O<sub>2</sub> = 26/4), namely, a transition state, laid between the metal and oxide sputtering mode, appeared in the deposition rate curve, where the film composition could be assumed to change obviously.

Figure 1c shows the color of the SnO<sub>x</sub> films deposited with different Ar/O<sub>2</sub> flow ratios but possessing similar thicknesses of ≈130 nm; it could be seen that the films deposited with low O<sub>2</sub> flow ratios (O<sub>2</sub> ≤ 2 sccm) were opaque because of the high metallic Sn content, whereas the films deposited with high O<sub>2</sub> flow ratios (≥4 sccm) were transparent for the increased Sn–O ingredient [20]. Moreover, Figure 1d demonstrates the optical transmittance spectra and shows an increased transparency with the increase in O<sub>2</sub> flow ratios; three curves corresponding to the low O<sub>2</sub> flow ratios (O<sub>2</sub> ≤ 2 sccm) were almost overlapped, and the film deposited with O<sub>2</sub> = 4 sccm especially corresponded to the turning point of the optical properties. A steep absorption edge appeared at a wavelength of about 450 nm for the films deposited with high O<sub>2</sub> flow ratios. The “blue shift” phenomenon of absorption edge occurred with the increase in oxidation degree, since the band gap of the films deposited with low O<sub>2</sub> flow ratios was small [25,26], which was caused by the doping energy levels in the Sn oxides [27,28].

XRD patterns of the SnO<sub>x</sub> films deposited on the glass substrate are shown in Figure 1e, since the signals from the Cu foil substrate disturbed the diffraction peaks largely. Then, the detected peaks were compared with the Powder Diffraction Files (PDF 04–0637 and 04–0673) of the crystal Sn and SnO<sub>2</sub> [29]. It was confirmed that the films deposited with low O<sub>2</sub> flow ratios (≤2 sccm) possessed obvious peaks located at 30.6°, 32.2°, 43.9°, 44.9°, 55.3° and 63.8°, all of which were ascribed to the lattice planes of 200, 101, 220, 211, 301 and 400 from metallic Sn, respectively, and its grain size was calculated using Scherrer’s equation; see Figure 1f. In the case of the films deposited with Ar/O<sub>2</sub> = 26/4,

the diffraction peaks completely disappeared and this could be explained by the increased oxidation degree [30]; next, the other three amorphous SnO<sub>x</sub> films were obtained when the O<sub>2</sub> flow ratios increased to 5, 6 and 7 sccm. The above XRD patterns demonstrated the disappearance tendency of the Sn crystals with the increase in O<sub>2</sub> flow ratios; the reasons for the amorphous structures are as follows: (1) the SnO<sub>x</sub> grain size was too small to be detected when compared with the X-ray coherence length; (2) the weak crystalline signal from SnO<sub>x</sub>, such as (110), was covered by the substrate peak positioned at 15°–32° [31]; (3) and the most likely reason is that the deposited materials had low reactivity and could not be arranged in an orderly manner when the substrate was not artificially heated [32]. It is worth noting that the amorphous structure could cause the volumetric strain introduced by alloying/dealloying reactions to be distributed evenly and avoid the local strain in a specific direction for crystal materials.

The SEM images of the as-grown SnO<sub>x</sub> films are shown in the left part of Figure 2. The SnO<sub>x</sub> films deposited with low O<sub>2</sub> flow ratios (O<sub>2</sub> ≤ 2 sccm) showed particle morphology; for instance, the film deposited with Ar/O<sub>2</sub> = 30/0 possessed irregularly shaped particles, and its minimum and maximum particle sizes were equal to 100 and 400 nm, respectively. Then, the particles transformed into sphere-like shapes, and the average particle size decreased from 80 to 30 nm when O<sub>2</sub> flow ratios increased from 1 to 2 sccm; these particles are proved to be composed of metallic Sn by the EDS information in Figure S2. However, the above particle morphology changed into a smooth surface when the O<sub>2</sub> flow ratio exceeded 4 sccm, as shown in Figure 2d–g; a smooth and dense accumulation film occurred, and no obvious particle was directly observed under the same SEM magnification. The reason for these obvious metallic Sn particles in the films deposited with low O<sub>2</sub> flow ratios (O<sub>2</sub> ≤ 2 sccm) is that a large number of Sn particles were sputtered on the substrate, and the particles had strong mobility to form large clusters. However, for the films deposited with relatively high O<sub>2</sub> flow ratios, the sputtered Sn particles were quickly oxidized, and the Sn–O bonds were formed; therefore, these films exhibited the characteristics of typical amorphous oxide material. Furthermore, the particles measured by SEM (Figure 2h) had a larger average size than that derived from the XRD in Figure 1f, which is attributed to the significant agglomeration of the particles (secondary particles) [33,34].

For the films after performing cycling, many cracks appeared on SnO<sub>x</sub> films after 20 cycles, as shown in the right part of Figure 2. In Figure 2a', the film deposited with Ar/O<sub>2</sub> = 30/0 retained a small amount of metal Sn. In Figure 2b' and c', the films deposited with low O<sub>2</sub> flow ratios (O<sub>2</sub> = 1, 2 sccm) broke into irregular shapes; obvious cracks (greater than 200 nm in width) and separated "islands" (the size is close to 1 μm) occurred. As for the films deposited with high O<sub>2</sub> flow ratios (O<sub>2</sub> ≥ 4 sccm) in Figure 2d'–g', two kinds of cracks occurred, one type of crack had a longer size and broke up the whole film into many "islands", and the crack length would become shorter as the O<sub>2</sub> flow ratios increased; the other type of crack had a smaller size (30 nm in width) and separated the residual part into smaller particles, and these particle size decreased from 46 to 20 nm as the O<sub>2</sub> flow ratios increased. All cracks were caused by the tensile stress introduced by the conversion reaction (SnO<sub>x</sub> + Li<sup>+</sup> + e<sup>-</sup> → Sn + Li<sub>2</sub>O) during the initial lithiation process, because metallic Sn exhibited a volume of 27 Å<sup>3</sup>, while SnO and SnO<sub>2</sub> had volumes of 36 Å<sup>3</sup> and 35 Å<sup>3</sup>, respectively [35]; it could be concluded that metallic Sn occupies 35% less volume compared to SnO<sub>x</sub>, and the reduced volume is the ultimate origin of tensile stress. Meanwhile, the element rearrangement could also be characterized using EDS information (Figure S3); it was found that the residual "islands" were mainly composed of Sn elements, and their distribution was consistent with the "islands" contour; there were no other kinds of elements detected in the crack positions. The Sn element rearrangement was likely a consequence of the high mobility [28] of the nanoscale Sn particles formed in the conversion reaction and the high mobility of Li<sup>+</sup> in the Li<sub>x</sub>Sn alloy (diffusion constants between 10<sup>-7</sup> and 10<sup>-8</sup> cm<sup>2</sup>/s [36]). Recently, researchers have introduced work function (WF) as a parameter to study the stability of electrodes [37–41]. The WF (Φ) is usually defined as the energy required to take away one electron from the Fermi level (μ), namely,

$\Phi = \varphi - \mu$ , where  $\varphi$  refers to the vacuum level. In the case of  $\text{VO}_x$ , the WF increases simultaneously with the oxidation state ranging from the value of 4.3 eV of the pure vanadium up to  $\approx 7$  eV as in stoichiometric  $\text{V}_2\text{O}_5$  [38]. Therefore, WF could also be used as a monitoring parameter to determine the stabilization of electrodes. For instance, metallic lithium could be implemented as an anode in a Li-based battery. The observed decrease in the WF indicates an increase in the Fermi energy relative to the vacuum level, with an inevitably enhanced energy drive for the treated surface to lose electrons and reduce interacting species. For another anode,  $\text{LiTiO}_2$ , the O vacancies on the surface decrease the WF and promote the interface reaction, the presence of O vacancies on the surface increases the electrons on the surface Ti ions, resulting in the presence of  $\text{Ti}^{3+}$  or other Ti ions with even lower valences. As a result, the WF decreases, easing the loss of electrons on the surface [39]. In conclusion, WF is an important parameter in Li-based batteries to improve electrode/electrolyte interface reactions.

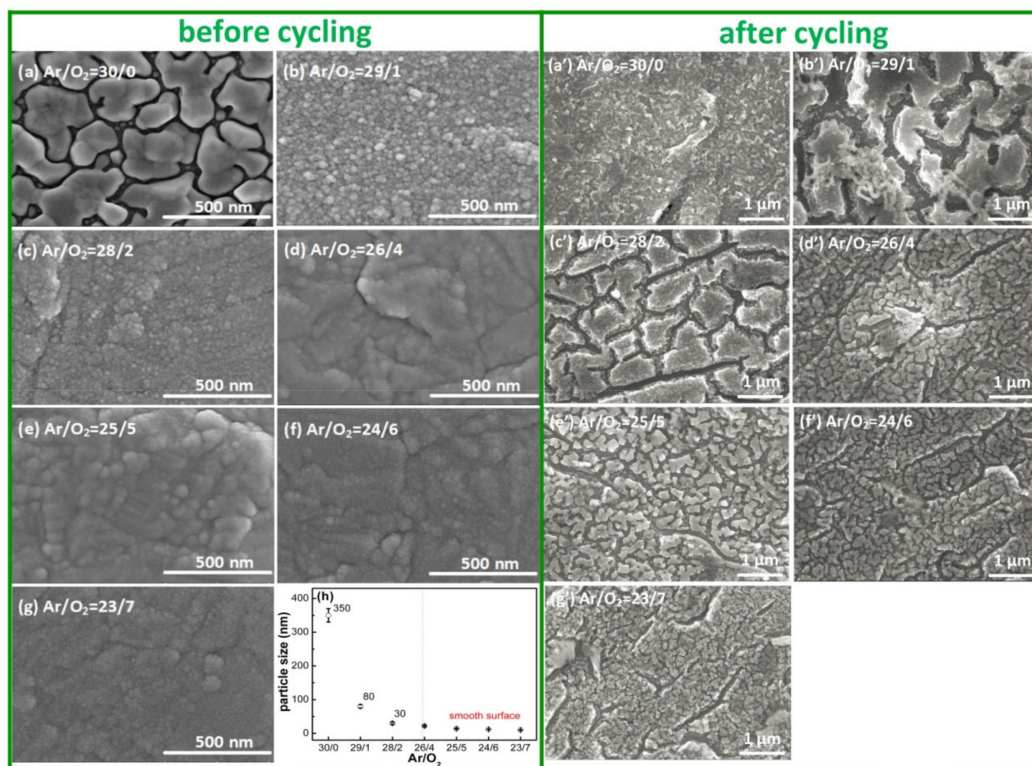


**Figure 2.** The surface SEM images of the  $\text{SnO}_x$  films before and after cycling, deposited with different  $\text{Ar}/\text{O}_2$  flow ratios: (a,a')  $\text{Ar}/\text{O}_2 = 30/0$ , (b,b')  $\text{Ar}/\text{O}_2 = 29/1$ , (c,c')  $\text{Ar}/\text{O}_2 = 28/2$ , (d,d')  $\text{Ar}/\text{O}_2 = 26/4$ , (e,e')  $\text{Ar}/\text{O}_2 = 25/5$ , (f,f')  $\text{Ar}/\text{O}_2 = 24/6$  and (g,g')  $\text{Ar}/\text{O}_2 = 23/7$ , and (h) represents the average particle size on  $\text{SnO}_x$  films.

In order to determine the deposited film quality and calculate the mass specific capacity later, X-ray reflectance (XRR) was adopted to measure the film density. First, Figure 3a shows the relationship between the surface roughness and the  $\text{Ar}/\text{O}_2$  flow ratios. This demonstrates that the film deposited with  $\text{Ar}/\text{O}_2 = 30/0$  possessed the highest roughness of  $50.0 \pm 7.0$  nm, and the roughness sharply decreased to  $4.6 \pm 0.2$  nm and stabilized at  $3.7 \pm 0.1$  nm with the increase in  $\text{O}_2$  flow ratios. Second, Figure 3b–g show the fitting results of the periodic oscillation curve; black dots represent the original experimental points, and the red curve signifies the fitting curve, exhibiting excellent consistency with the original data. The films deposited with the condition of  $\text{O}_2 \geq 2$  sccm possessed roughness of less than 4.5 nm; their reflectance curves shown in Figure 3c–g had periodic oscillation characteristics and could be fitted, the fitting thickness was close to the actual thickness of 130 nm and its relative deviation was less than 8%; the fitting roughness also distributed in the interval of 3.07–4.22 nm, consistent with the roughness results characterized by AFM in

Figure 3a and Figure S4. Lastly, the fitting density decreased from 6.58 to 6.20 g/cm<sup>3</sup> when the O<sub>2</sub> flow ratios increased from 2 to 7 sccm. The film density was proportional to the critical angle  $\theta_c$  in the reflectance curve, and  $\theta_c$  showed a decreasing trend as the O<sub>2</sub> flow ratios increased, confirming the decreased trend of film density displayed in Figure 3h. The film density results fitted by the model shown in Figure S5 was close to that of the SnO<sub>2</sub> films prepared by the atomic layer deposition (ALD) method [28], but still smaller than the bulk densities of SnO of 6.45 g/cm<sup>3</sup> [42] and SnO<sub>2</sub> of 6.38 g/cm<sup>3</sup> [43]. Third, the films deposited with low O<sub>2</sub> flow ratios had roughness of larger than 4.5 nm, which would cause X-ray scattering and disturb periodic oscillation signals; therefore, the film density could not be directly fitted by the XRR model in Figure S5. The weighing method was then applied, and the densities were calculated to be 7.20 and 6.69 g/cm<sup>3</sup>, respectively. Finally, the values of film density are summarized in Figure 3h; they were always less than the corresponding density of bulk material. For example, the density of the Sn film deposited at Ar/O<sub>2</sub> = 30/0 was smaller than 7.29 g/cm<sup>3</sup> of the bulk metallic Sn<sup>0</sup>, which is because the films deposited with the MS method could not reach 100% close packing state; there were many gaps within the as-grown films, as shown in Figure 2. The deposited films belonged to Sn oxides with oxygen vacancy, and the actual densities of the films deposited at various O<sub>2</sub> flow ratios were lower than the theoretical density.

### 3.2. Composition of the SnO<sub>x</sub> Films

The types of elements contained in the SnO<sub>x</sub> films were determined to be C, Sn and O according to the survey spectrum shown in Figure S6. The Sn 3d spectrum is presented in Figure 4a; the Sn 3d core level peak was composed of double peaks, corresponding to Sn 3d<sub>3/2</sub> and Sn 3d<sub>5/2</sub> at ≈495.0 and ≈486.6 eV, respectively. Furthermore, the spin-orbit splitting between the two peaks was close to 8.4 eV, consistent with the energy levels reported for SnO<sub>2</sub> [44]. Additionally, it was noted that the SnO<sub>x</sub> films deposited with low O<sub>2</sub> flow ratios (O<sub>2</sub> ≤ 2 sccm) exhibited an obvious shoulder peak at a binding energy close to 485.0 eV, which corresponded to the Sn–Sn bond from metallic Sn<sup>0</sup> [6,14], and the peak area of Sn<sup>0</sup> gradually decreased with the increase in O<sub>2</sub> flow ratios. The existence of Sn<sup>2+</sup> and Sn<sup>4+</sup> components was further confirmed by the fitting procedure of the Sn 3d<sub>5/2</sub> peak. The Sn 3d<sub>5/2</sub> peak can be divided into two peaks corresponding to Sn<sup>2+</sup> (binding energy of 487.2 eV) and Sn<sup>4+</sup> (486.4 eV) [15,45–47], indicating the coexistence of the SnO and SnO<sub>2</sub> phases; the energy separation of ≈0.8 eV between Sn<sup>2+</sup> and Sn<sup>4+</sup> is interpreted as a chemical shift [44], located in the range of 0.5–0.8 eV, pointed out by the literature [6,48]. It was also noted that the peak position of Sn 3d shifted to a lower binding energy, and the peak shape became gradually symmetrical when the O<sub>2</sub> flow ratios exceeded 4 sccm. Additionally, the film composition of the SnO<sub>x</sub> film deposited with Ar/O<sub>2</sub> = 26/4 was in a transition state, consisting of a mixture of Sn, SnO, SnO<sub>2</sub>.

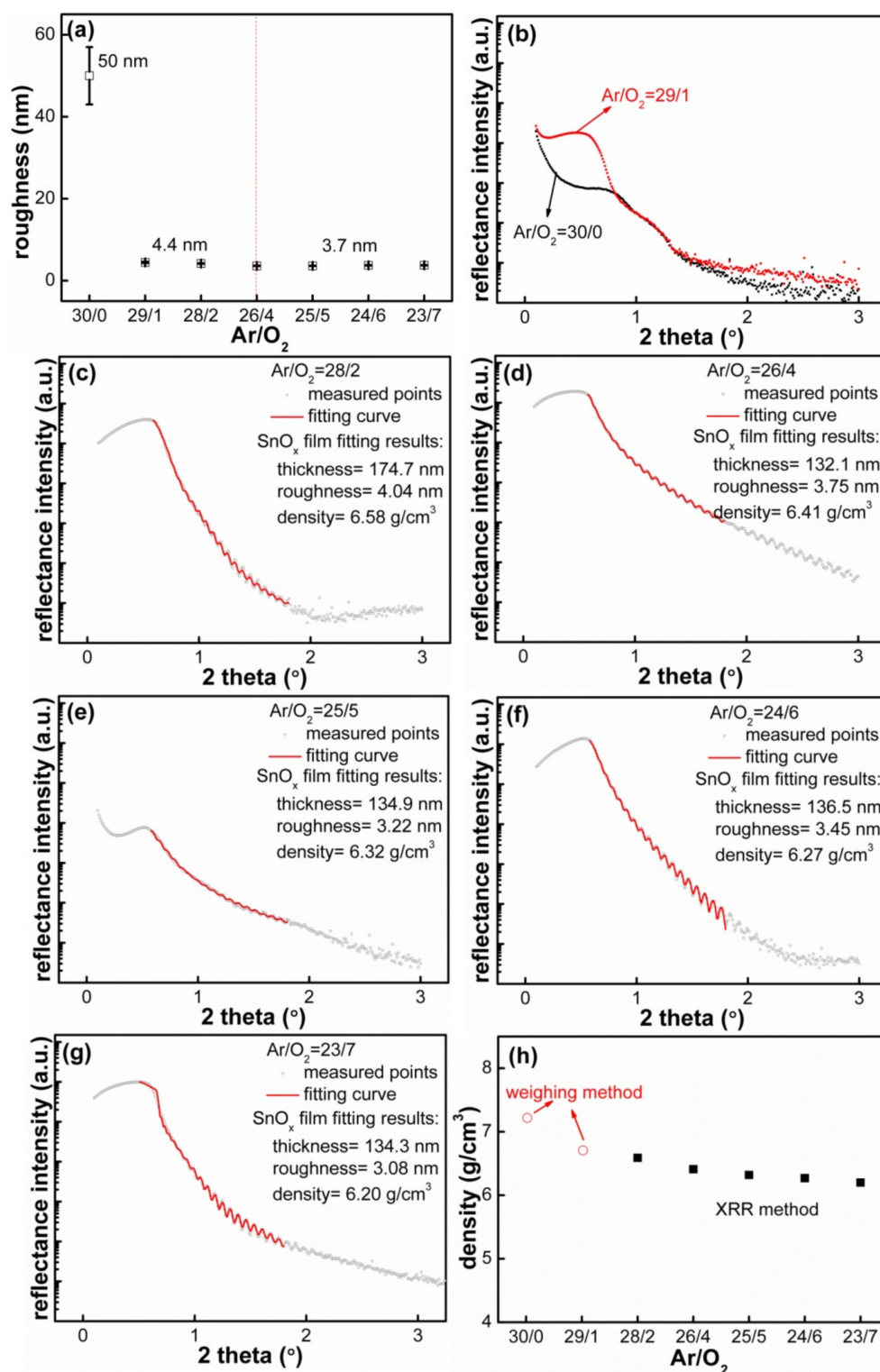
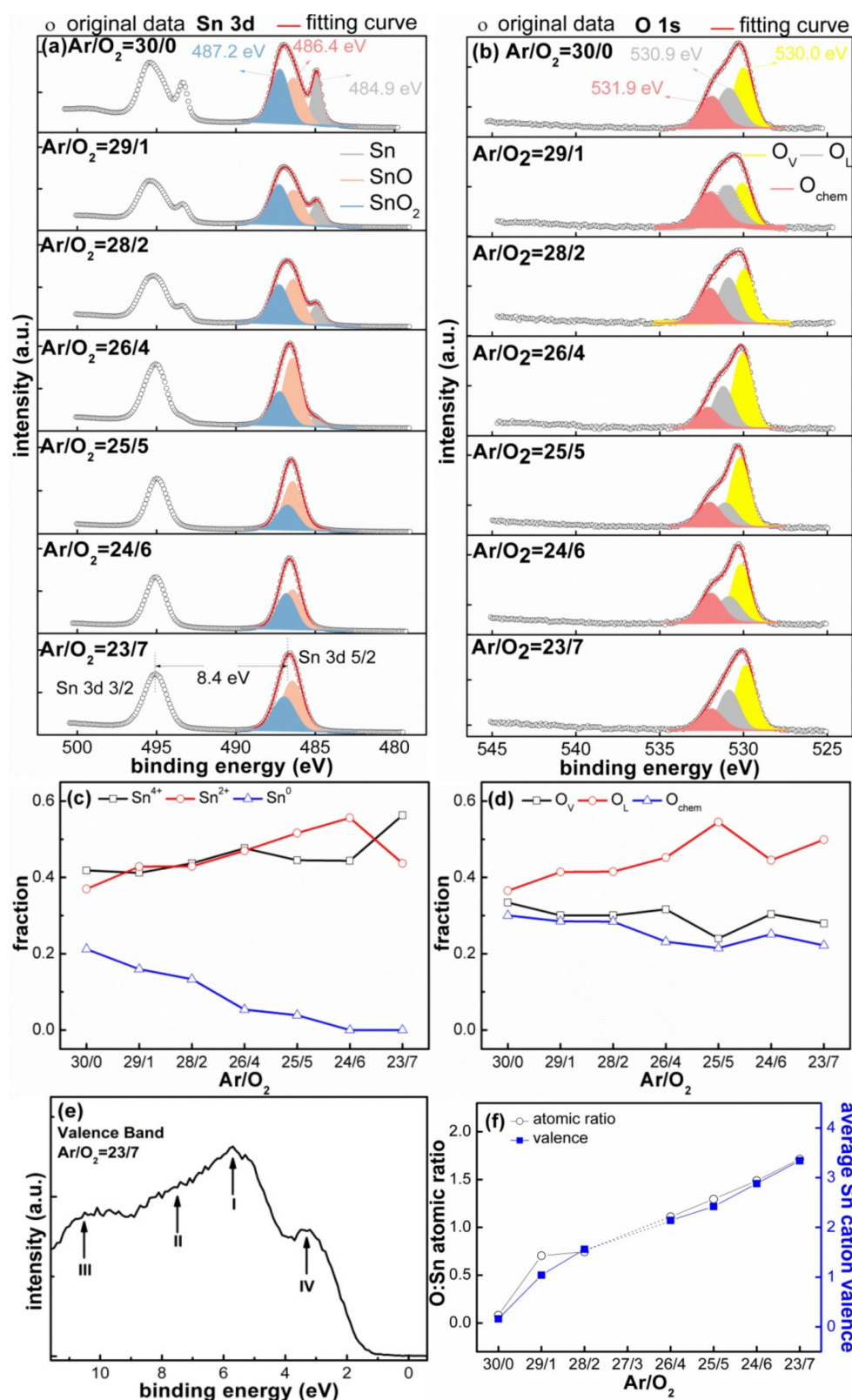


Figure 3. (a) Summary of the surface roughness measured by AFM; (b) the reflectance curves of the films deposited with Ar/O<sub>2</sub> = 30/0 and 29/1; the reflectance curves and fitting results of the films deposited with (c) Ar/O<sub>2</sub> = 28/2, (d) Ar/O<sub>2</sub> = 26/4, (e) Ar/O<sub>2</sub> = 25/5, (f) Ar/O<sub>2</sub> = 24/6 and (g) Ar/O<sub>2</sub> = 23/7; (h) the film density as a function of Ar/O<sub>2</sub> flow ratios.





**Figure 4.** (a) Sn 3d and (b) O 1s spectra of the SnO<sub>x</sub> films deposited with different Ar/O<sub>2</sub> flow ratios; the relative content of (c) Sn and (d) O with increased O<sub>2</sub> flow ratios; (e) valence band spectrum; (f) summary of the O:Sn atomic ratios and average Sn cation valence.

As shown in Figure 4b, a decomposition procedure of O 1s core level peak was performed to analyze the oxidation degree; it was observed that the O 1s peak in the

SnO<sub>x</sub> films deposited with low O<sub>2</sub> flow ratios (O<sub>2</sub> ≤ 2 sccm) was wide, asymmetrical and had a significant shoulder at the higher binding energy (≈532.0 eV) side, while the peak shape gradually became symmetrical when the O<sub>2</sub> flow ratios increased. According to the peak fitting results, the following conclusions were obtained: (1) The oxygen elements at the shoulder position belong to the chemisorbed oxygen (O<sub>chem</sub>), such as hydroxyl ions (OH<sup>-</sup>) [42,45,49,50], and the presence of O<sub>chem</sub> is not surprising when considering the film morphology with microgaps (like in Figure 2), which can allow gaseous contaminants to attach onto internal particles within the film. Moreover, two oxidation states corresponding to the Sn<sup>4+</sup> (SnO<sub>2</sub>) and Sn<sup>2+</sup> (SnO) are easily distinguished. (2) The oxygen element at the dominant peak of ≈530.9 eV comes from lattice oxygen (O<sub>L</sub>), namely, the Sn–O–Sn bond [42,44]. (3) Another one resolved at ≈530.1 eV is associated with the O<sup>2-</sup> ions in the oxygen-deficient regions (O<sub>V</sub>) [48,51]; O<sub>L</sub> and O<sub>V</sub> are also separated by ≈0.8 eV, and this is attributed to the incomplete oxidation state [45]. This result suggests that the oxidation of the Sn component is incomplete under the selected Ar/O<sub>2</sub> atmosphere, leading to the coexistence of SnO and SnO<sub>2</sub> phases within the deposited films.

In fact, it was found that the peak positions in the films deposited with different Ar/O<sub>2</sub> flow ratios were not completely consistent. For example, the binding energies corresponding to Sn<sup>2+</sup> shifted, and the deviation among the different decomposition results was less than 0.2 V; this binding energy shift could be explained by the buried electrical potential model [52,53], which assumes that the deviation is derived from inhomogeneous charge distribution brought by the mixture composition (Sn, SnO and SnO<sub>2</sub>), the conductive mental Sn, nonconductive SnO<sub>2</sub> materials, as well as different surface roughness and porosity. All components together led to uneven charge distribution on the film surface, resulting in irregular peak shifts. Moreover, the SnO<sub>x</sub> films would inevitably come into contact with the air and form surface contamination before XPS testing, since the existing SnO<sub>2</sub> component is an n-type semiconductor, and the oxygen chemisorptions have a stronger affinity for electrons, so the electrons on the surface were captured and formed a space charge layer [54], which also caused the uneven distribution of the charges. Hence, we performed an Ar<sup>+</sup> etching experiment [55] and the XPS spectra of the SnO<sub>2</sub> standard material to calibrate the O:Sn atomic ratios, as shown in Figures S7 and S8.

An additional valence band (VB) was further selected to identify the oxidation degree. For instance, the VB spectrum of the sample deposited at Ar/O<sub>2</sub> = 23/7 is displayed in Figure 4e, and four peaks occurred: (1) the first peak at the binding energy of ≈5.0 eV (I) is ascribed to the O 2p bonding or nonbonding characteristic; (2) intermediate states around 7.5 eV (II) originate mainly from hybridization between Sn 5p and O 2p orbital; (3) the lower part of VB around 10.6 eV (III) is due to the strong interaction between Sn 5s and O 2p orbital, and above three peaks are fingerprints of SnO<sub>x</sub> [56]; (4) a small band gap state between 2.0 and 4.0 eV (IV) with respect to the Fermi edge was also observed, which is attributed to the band gap states in the SnO<sub>2</sub> [57–59]. Therefore, we can conclude from this VB measurement that the above SnO<sub>x</sub> films deposited by different Ar/O<sub>2</sub> atmospheres contain a mixture phase of Sn<sup>4+</sup> and Sn<sup>2+</sup>.

In order to quantify the oxidation degree (x) in the SnO<sub>x</sub> film, we used the peak fitting results and factor analysis method (namely, formula 1.1) to calculate the relative content and average valence. The related literature [60,61] have introduced calculating procedures by the atomic sensitivity factor (ASF); for instance, Kwoha et al. [62] calculate the relative O:Sn concentration in SnO<sub>2</sub> films based on the ASF. In Figure 4c and d, the relative content of Sn<sup>0</sup> decreased linearly from 16% to 0%, and the content of Sn oxides (Sn<sup>2+</sup>, Sn<sup>4+</sup>) increased when the Ar/O<sub>2</sub> flow ratios changed from 29/1 to 23/7; the higher the O<sub>2</sub> partial pressure is, the greater the formation of O<sub>L</sub> and O<sub>V</sub> is; the relative content increased from 70% to a stable value of 80% as the O<sub>2</sub> flow ratios increased. Next, the O:Sn atomic ratios as a function of Ar/O<sub>2</sub> flow ratios is summarized in Figure 4f; the values of the O:Sn ratio increased by ≈0.19 when the O<sub>2</sub> flow rate increased by 1 sccm. The SnO<sub>x</sub> films deposited with low O<sub>2</sub> flow ratios (O<sub>2</sub> ≤ 2 sccm) possessed a composition of SnO<sub>0.70</sub> and SnO<sub>0.74</sub>, respectively, and the O:Sn value was less than 1.0 due to the presence

of metal Sn, consistent with the above XRD and SEM results. Specially, the detected oxygen component in the metallic Sn film deposited with Ar/O<sub>2</sub> = 30/0 likely resulted from the surface oxidation when it transferred through air for the XPS measurement [63]. While other films deposited with high O<sub>2</sub> flow ratios (O<sub>2</sub> ≥ 5 sccm) retained the film composition of SnO<sub>1.30</sub>, SnO<sub>1.48</sub> and SnO<sub>1.71</sub>, the O:Sn value was greater than 1.0 due to the increased oxidation state. The formation of SnO<sub>1.09</sub> was measured for the film deposited at Ar/O<sub>2</sub> = 26/4, belonging to a special transition state. However, a thoroughly oxidized SnO<sub>2</sub> film could not be obtained under the selected Ar/O<sub>2</sub> atmosphere conditions; this is restricted by the characteristics of the MS process. The introduced reactive O<sub>2</sub> as an oxygen source was easily pumped away in the sputtering chamber, which reduced the contact with the sputtered Sn particles; meanwhile, the films deposited by the Ar/O<sub>2</sub> mixture gas tended to be in an oxygen-deficient state owing to insufficient decomposition of O<sub>2</sub> [20].

$$x = \frac{n_{\text{O}}}{n_{\text{Sn}}} = \frac{I_{\text{O}}/ASF_{\text{O}}}{I_{\text{Sn}}/ASF_{\text{Sn}}} \quad (1)$$

where the stoichiometry  $x$  is equal to  $n_{\text{O}}/n_{\text{Sn}}$ , representing the atomic ratio; the letter  $I$  denotes the intensity of the photoelectron (namely, refers to the peak area of a characteristic peak), which has a linear relationship with the atomic concentration in the sample; and the ASF values for Sn and O were confirmed to be 4.095 and 0.711, respectively, according to the library of ASF in the XPS apparatus.

### 3.3. Electrochemical Performance of the SnO<sub>x</sub> Films

The choice of potential window is crucial for Sn-based compounds to realize high performance, and the influence of different O:Sn atomic ratios on its electrochemical reaction process is still not clear; hence, CV was conducted to study the reaction mechanism for SnO<sub>x</sub>/electrolyte/Li configuration, as presented in Figure 5. All CV curves were measured at a scan rate of 0.1 mV/s between 0.01 and 2.0 V. In order to eliminate the interference from the Cu foil substrate during the electrochemical reaction, Figure 5a first shows the CV curve of bare Cu foil with the same characterized condition, and no reduction/oxidation peaks occurred, which indicates that the Cu foil remained electrochemically inert and did not participate in any reaction under this measurement condition. Then, the other CV curves presented in Figure 5 revealed the electrochemical reaction trend between Li and SnO<sub>x</sub> when the SnO<sub>x</sub> evolved as follows: “metallic Sn → oxide deficient → oxide rich”.

First, the CV curves of SnO<sub>x</sub> films deposited with low O<sub>2</sub> flow ratios (O<sub>2</sub> ≤ 2 sccm) were similar to that of the metallic Sn, exhibiting the independent and sharp peak characteristics just like in Figure 5b–d. Four reduction peaks appeared at 1.65, 0.67, 0.55 and 0.40 V during the first reduction (lithiation) process; the peak at 1.65 V disappeared in the following cycles, and it is ascribed to the decomposition of the electrolyte (the electrolyte is reduced into impurities, such as Li<sub>2</sub>CO<sub>3</sub> [42]) and the formation of the SEI layer; the reduction peaks at the other three positions corresponded to the Li–Sn alloying reactions, it would form Li–Sn alloys with a high lithium content. While in the following oxidation (delithiation) process, four oxidation peaks appeared at 0.45, 0.60, 0.71 and 0.79 V, respectively, the Li<sub>x</sub>Sn alloy could be in a complete delithiation state when the potential increased to ≈1.0 V. As for the second cycle process, two reduction peaks at 0.67 and 0.55 V merged into one reduction peak at 0.62 V, indicating that the electrode structure changed after the first cycle, but the four oxidation peaks hardly changed and corresponded to the delithiation process of Li<sub>22</sub>Sn<sub>5</sub>, Li<sub>7</sub>Sn<sub>2</sub>, Li<sub>7</sub>Sn<sub>3</sub> and LiSn [64].

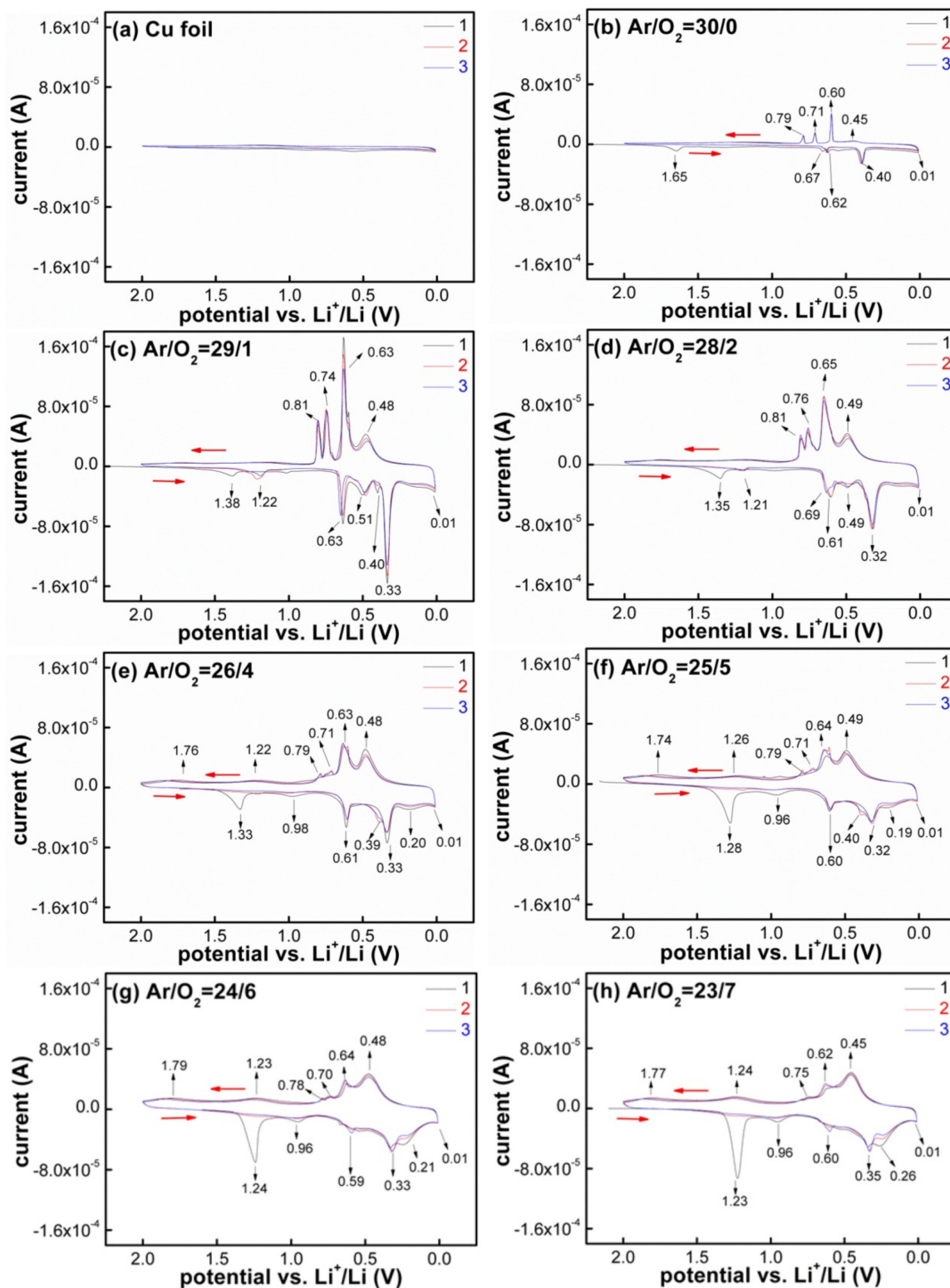
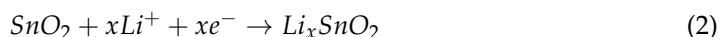


**Figure 5.** CV curves of the  $\text{SnO}_x$  films deposited with different  $\text{Ar}/\text{O}_2$  flow ratios: (a) bare Cu foil, (b) 30/0, (c) 29/1, (d) 28/2, (e) 26/4, (f) 25/5, (g) 24/6 and (h) 23/7.

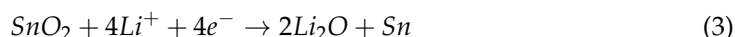
Second, the  $\text{SnO}_x$  films deposited with high  $\text{O}_2$  flow ratios ( $\text{O}_2 \geq 4$  sccm) contained electrochemical conversion reaction due to the obvious existence of oxides. The CV curves of the initial three cycles are shown in Figure 5e–h. Taking the film deposited with the condition of  $\text{Ar}/\text{O}_2 = 23/7$  as an example, during the first cathodic sweep, the CV traces showed the structural destruction of  $\text{SnO}_x$  above 1.0 V vs.  $\text{Li}/\text{Li}^+$  [65]; the broad peaks at

1.23 and 0.96 V represented the decomposition of the electrolyte to form the SEI layer and the conversion reaction of  $\text{SnO}_x$ , namely, the formation of intermediate  $\text{Li}_x\text{SnO}_2$  phase [6] first, and then reduced into metallic  $\text{Sn}^0$  particles as shown in formula 1.2 and 1.3 [3,66]. Three other reduction peaks at 0.60, 0.35 and 0.26 V corresponded to the  $\text{Li}^+$  insertion into the Sn structural lattice to form  $\text{Li}_x\text{Sn}$  alloys, such as  $\text{Li}_{0.4}\text{Sn}$ ,  $\text{LiSn}$  and  $\text{Li}_{2.33}\text{Sn}$ , according to formula 1.4 [3]. In the first anodic sweep, oxidation peaks at 0.45, 0.62 and 0.75 V corresponded to the delithiation reactions of  $\text{Li}_x\text{Sn}$  alloys at different stages; these peaks agree well with those given in the metallic Sn [29], and two additional broad peaks at 1.24 and 1.77 V occurred in the oxygen-rich  $\text{SnO}_x$  films. These two newly appeared oxidation peaks corresponded to the partially reversible delithiation reaction of  $\text{Li}_2\text{O}$  [42]. In subsequent cycles, two cathodic peaks at 1.23 and 0.96 V disappeared, and the other three cathodic peaks were replaced with less intense ones along with the peak position shifts to the low potential direction, which was caused by the increase in battery internal resistance. The battery internal resistance came from two aspects: (1) the formation of  $\text{Li}_2\text{O}$  during the first lithiation, which is not a good electronic conductor [29], (2) many cracks appeared after cycling; the electrochemically active materials around the crack positions lost electrical contact and formed new SEI layers; the thick SEI layer predominantly contained inorganic products, such as  $\text{LiF}$  and  $\text{Li}_2\text{CO}_3$ , and led to a large resistivity [67]. While in the following oxidation process, the intensity of the three peaks remained unchanged, except for the intensity of the oxidation peak positioned at 0.62 V. The CV curves after the first cycle were completely consistent with each other, indicating a good reversibility for the  $\text{SnO}_x$  film electrodes.

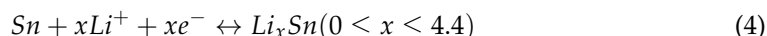
Insertion (intermediate phase):



Conversion: (>1.2 V vs.  $\text{Li}/\text{Li}^+$ , with capacity of  $\approx 711$  mAh/g):



Alloying/dealloying: (<0.5 V vs.  $\text{Li}/\text{Li}^+$ , with capacity of  $\approx 783$  mAh/g):



Comparing the above CV curves shown in Figure 5, we could notice that the changes in electrochemical reaction revealed a transition from “single alloying” mode to “conversion + alloying” mode owing to the composition transition from “oxide deficient” to “oxide rich” [6]. The core difference in the electrochemical reaction between Sn and  $\text{SnO}_x$  is also given: (1)  $\text{SnO}_x$  films possessed a characteristic reduction peak in the voltage range of 1.3–0.9 V, and the intensity of this peak increased with oxidation degree. This position corresponded to the formation of the SEI layer in the  $\text{SnO}_x$  material and was very different from that in the Sn material. The metallic Sn provided a high voltage of 1.6–2.5 V for SEI formation, which has been testified by an in situ AFM observation [68]. (2) The reduction peaks located in the range of 0.80–0.01 V corresponded to a series of Li–Sn alloying reactions, and the peak shape changed abnormally with the increase in the cycle numbers. For example, the  $\text{SnO}_x$  film deposited at the condition of  $\text{Ar}/\text{O}_2 = 26/4$  (Figure 5g) showed a special peak at 0.21 V, and its intensity increased with the cycle number particularly; this is explained by the cluster growth of metallic Sn nanoparticles. The formed Sn nanoparticles after the first cycle agglomerated during the following charge/discharge process due to its good mobility. (3) New oxidation peaks appeared above 1.0 V, which are ascribed to the statement that “ $\text{Li}^+$  are partly released by  $\text{Li}_2\text{O}$ ”; this view has been proved by Mössbauer spectroscopy [42,69] and could be used to explain why the first discharge capacity of  $\text{SnO}_x$  was higher than the theoretical capacity.

Lastly, it was noted that the CV curves measured by the  $\text{SnO}_x$  electrodes were different from those from  $\text{SnO}_x$  powder materials in the literature. More peak signals could be

detected in the film electrode, and this film anode is more likely to be an ideal model for analyzing reaction mechanisms. The reaction mechanism of  $\text{SnO}_x$  was confirmed as follows. The electrolyte solution and  $\text{Li}^+$  first reacted at the interface of the  $\text{SnO}_x$ /electrolyte to form SEI layers; then, the  $\text{Li}^+$  passed through the SEI layer and penetrated into the  $\text{SnO}_x$  to form intermediate  $\text{Li}_x\text{SnO}_2$ .  $\text{Li}_x\text{SnO}_2$  converted into metallic Sn nanoparticles and the  $\text{Li}_2\text{O}$  matrix quickly. Next,  $\text{Li}^+$  and the newly formed metallic Sn nanoparticles carried out a series of alloying reactions to form the  $\text{Li}_x\text{Sn}$  alloy along with  $\text{Li}_2\text{O}$  distributed around them. During the dealloying process, the  $\text{Li}_x\text{Sn}$  alloy was completely delithiated at a voltage below 1.0 V, and even part of  $\text{Li}_2\text{O}$  was reversibly delithiated when the delithiation voltage was higher than 1.0 V.

The initial discharge/charge curves of all  $\text{SnO}_x$  film electrodes are compared in Figure S9. The curves exhibited the following two characteristics when  $\text{O}_2$  flow ratios increased: (1) The  $\text{SnO}_x$  films deposited with low  $\text{O}_2$  flow ratios ( $\text{O}_2 \leq 2$  sccm) had a series of obvious potential platforms below 1.0 V, coinciding well with the oxidation/reduction peaks in the above CV curves. However, the  $\text{SnO}_x$  films deposited with high  $\text{O}_2$  flow ratios ( $\text{O}_2 \geq 4$  sccm) only showed sloping curves without obvious potential platforms. (2) New platforms located at  $\approx 1.2$  V were only detected in the  $\text{SnO}_x$  films deposited with high  $\text{O}_2$  flow ratios ( $\text{O}_2 \geq 4$  sccm), which indicates a conversion reaction. In addition, all  $\text{SnO}_x$  electrodes showed drastic irreversible capacity ( $\approx 50\%$ ), such as the  $\text{SnO}_{1.68}$  film deposited at  $\text{Ar}/\text{O}_2 = 23/7$ , the initial discharge/charge capacity of which was equal to 1035.2/507.1 mAh/g, corresponding to a small coulomb efficiency of 49.0%. Generally, huge irreversible capacity loss in  $\text{SnO}_x$  is attributed to the irreversible  $\text{Li}^+$  loss from the formation of SEI and  $\text{Li}_2\text{O}$  [28]. The phenomenon that the detected discharge capacity ( $>1000$  mAh/g) is larger than the theoretical capacity (782.0 mAh/g) of  $\text{SnO}_2$  could be explained by the selected cut-off potential of 1.2 V exceeding 0.8 V vs.  $\text{Li}/\text{Li}^+$ , which causes some  $\text{Sn}^0$  nanoparticles to not be oxidized into  $\text{SnO}_2$ , namely, the maximum binding of 6.4 mol of  $\text{Li}^+$  (theoretical capacity of  $\approx 1138$  mAh/g) [62].

Then, we compared the cycle performance of all  $\text{SnO}_x$  electrodes. The galvanostatic discharge/charge process was executed in a voltage range of 0.01–1.2 V at a current rate of  $44 \mu\text{A}/\text{cm}^2$ , and the results are shown in Figure 6. The left column represents the specific discharge/charge curves of the 1st, 2nd, 5th, 25th and 50th cycles; the right column represents the discharge capacity and coulomb efficiency as a function of cycle numbers. For the  $\text{SnO}_x$  films deposited with low  $\text{O}_2$  flow ratios ( $\text{O}_2 = 0, 1, 2$  sccm), the reversible capacity after 50 cycles could be delivered as 27.4, 47.3 and 166.4 mAh/g, respectively, while for the  $\text{SnO}_x$  films deposited with increased  $\text{O}_2$  flow ratios ( $\text{O}_2 \geq 4$  sccm), the relative stable capacity of 379.6, 359.6, 388.6 and 396.1 mAh/g could be delivered after 50 cycles; the maximum reversible capacity of 396.1 mAh/g and capacity retention ratio of 75.4% pertain to the  $\text{SnO}_{1.71}$  film deposited with  $\text{Ar}/\text{O}_2 = 23/7$ . The excellent cycle stability in the oxygen-rich film may be attributed to the stable structure and morphology introduced by the elevated oxidation degree. Its amorphous structure (Figure 1e) caused the film volume to expand in all directions uniformly, instead of an individual expansion in the crystal; the smooth surface (Figure 2) was conducive to uniform charge distribution and prevented the local expansion during the alloying/dealloying reactions; and the enhanced oxidation degree in  $\text{SnO}_x$  formed more  $\text{Li}_2\text{O}$  matrix during cycling. The evenly distributed  $\text{Li}_2\text{O}$  around Sn nanoparticles plays a very important role in allowing the electrode to expand and contract reversibly.

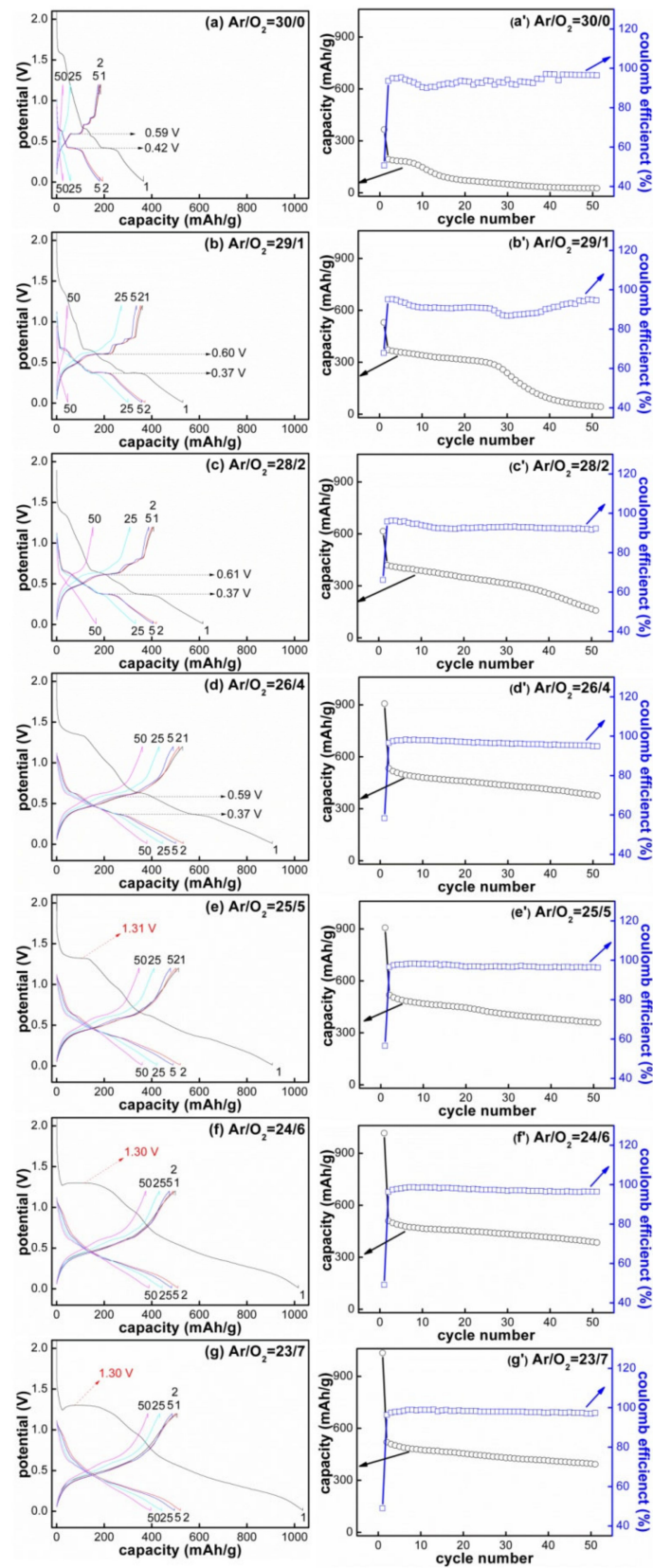


**Figure 6.** Cycling performance of the SnO<sub>x</sub> films deposited with different Ar/O<sub>2</sub> flow ratios: (a,a') 30/0, (b,b') 29/1, (c,c') 28/2, (d,d') 26/4, (e,e') 25/5, (f,f') 24/6 and (g,g') 23/7.

However, all SnO<sub>x</sub> film electrodes possessed a common phenomenon, namely, the discharge capacity decayed with the increase in cycle number. The comprehensive effects

of volume change and continuous SEI formation contributed to this capacity decay. The initial SEI layer was formed instantaneously when electrodes contact with the electrolyte solution [70], then the formed  $\text{Li}_x\text{Sn}$  alloys showed a severe volume expansion effect (up to 300%) and destroyed the entire membrane structure, so the fresh active material was continuously exposed to the electrolyte solution, resulting in further electrolyte decomposition and thick SEI layers [71,72]. Therefore, the reversible capacity did not stop decreasing until the film electrode formed a stable structure, covered by a thick SEI layer or decomposed into a critical size, which would prevent the continuous exposure of the fresh electrode to the electrolyte solution. To confirm our assumption about the relationship between capacity fading and volume change, the morphological evolutions of the  $\text{SnO}_x$  film after 20 cycles were also characterized in Figure 2b; the cracks were generated due to the huge volume variation of " $\text{Li}_{4.4}\text{Sn}$  ( $7738.9 \text{ \AA}^3$ )  $\leftrightarrow$   $\text{Sn}$  ( $108.2 \text{ \AA}^3$ )  $\leftrightarrow$   $\text{SnO}$  ( $69.8 \text{ \AA}^3$ )  $\leftrightarrow$   $\text{SnO}_2$  ( $71.5 \text{ \AA}^3$ )" [73,74] during the charge/discharge cycle; the destroyed electrode structure verified that the gradual decay of discharge capacity was related to the detachment of the active materials from the current collector [29].

Figure 7 showed the rate capabilities of the  $\text{SnO}_x$  films deposited with different  $\text{Ar}/\text{O}_2$  flow ratios, and these electrodes were continuously cycled without suspension among the progressive current densities ( $44 \rightarrow 176 \rightarrow 22 \mu\text{A}/\text{cm}^2$ ). The rate capability of the  $\text{SnO}_x$  films deposited with high  $\text{O}_2$  flow ratios ( $\text{O}_2 \geq 4 \text{ sccm}$ ) was better than that of the films deposited with low  $\text{O}_2$  flow ratios ( $\text{O}_2 \leq 2 \text{ sccm}$ ). For instance, the film deposited with  $\text{Ar}/\text{O}_2 = 23/7$  performed cycling at four increased current densities, 44, 88, 132,  $176 \mu\text{A}/\text{cm}^2$ , and carried out 10 cycles at each current density; the final discharge capacity was 412.0 mAh/g, and the capacity retention rate was 79.0%. However, the other electrode had a reversible discharge capacity of 414.1 mAh/g and a capacity retention rate of 79.5% when cycling at a constant current density of  $44 \mu\text{A}/\text{cm}^2$  after 40 cycles, which indicates that the increased current density had no obvious effect on the reversible discharge capacity. However, the film deposited with  $\text{Ar}/\text{O}_2 = 28/2$  only had a discharge capacity of 240.7 mAh/g and a capacity retention rate of 58.7% after 40 cycles. Moreover, the specific capacity did not recover as expected when the current density began to decrease at the 41st cycle. Taking the film electrode deposited with a condition of  $\text{Ar}/\text{O}_2 = 23/7$  as an example, it had a reversible discharge capacity of 405.4 mAh/g and a capacity retention rate of 77.8% after the following 30 cycles at the decreased current densities of 132, 88 and  $44 \mu\text{A}/\text{cm}^2$ . The reason for the improvement in the rate capability of the  $\text{SnO}_x$  films deposited with high  $\text{O}_2$  flow ratios is similar to that explaining the improved cycle performance: both could be attributed to the increased  $\text{Sn}^{4+}$  composition, which plays an important role in electrochemical performance improvement.

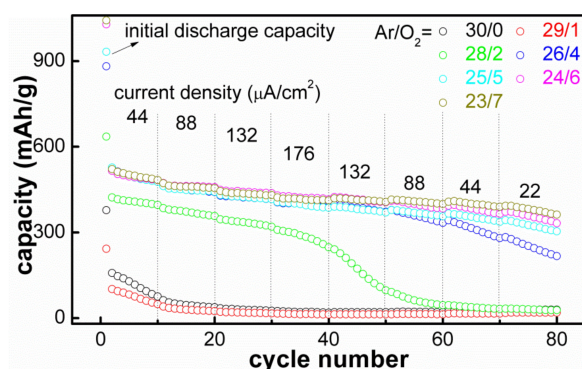
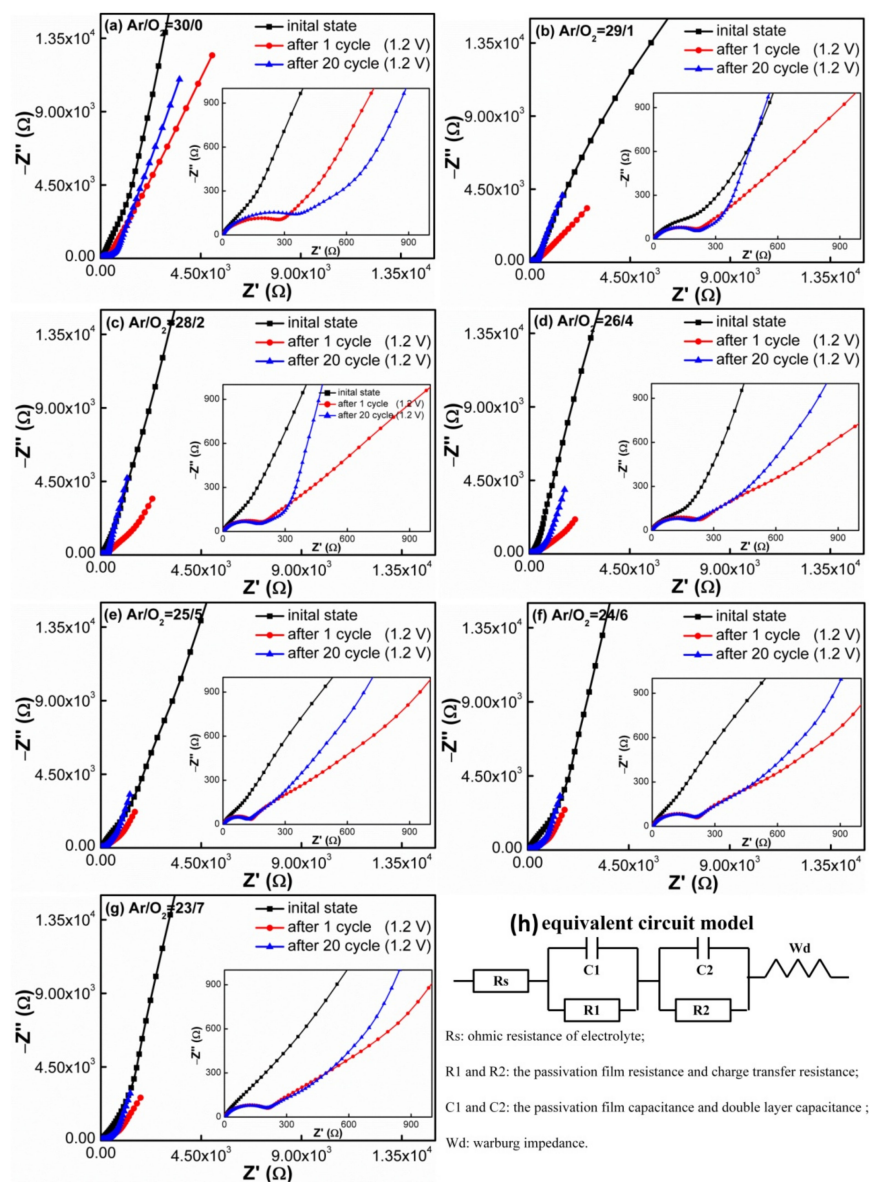


Figure 7. Rate performance of the  $\text{SnO}_x$  films deposited with different  $\text{Ar}/\text{O}_2$  flow ratios.

The impedance of all  $\text{SnO}_x$  electrodes at different cycling states was also shown in Figure 8. The EIS curves were measured before cycling, after 1 cycle and 20 cycles at 1.2 V vs.  $\text{Li}/\text{Li}^+$ . All curves were fitted with the same equivalent circuit models shown in Figure 8h. It was found that the Nyquist plots typically displayed a depressed semicircle at the high



frequency range, while the sloping line was at the low frequency range. In the equivalent circuit model,  $R_s$  is the ohmic resistance of the electrolyte, separator and electrode;  $R_1$  and  $C_1$  represent the resistance and capacitance of the SEI layer, respectively, corresponding to the semicircular arc in the high frequency region;  $R_2$  and  $C_2$  represent the double layer capacitance and passivation film capacitance, respectively;  $W_d$  represents the Warburg impedance caused by  $Li^+$  diffusion in the electrode, corresponding to the sloping line in the low frequency region [75,76]. As shown in Figure 8, the EIS patterns of the as-grown film electrodes had no semicircle, and the corresponding impedance was distributed in the range of 2.4–2.9  $\Omega$ , which is close to the ohmic impedance of the electrolyte. However, the EIS curves began to show an obvious semicircle, and the semicircle hardly changed with the increase in cycle number. Additionally, the impedance decreased with the gradual increase in  $O_2$  flow ratios, and the impedance changed from 246 to 130  $\Omega$ , which means that the cycled  $SnO_x$  had a lower charge transfer impedance than pure Sn. The faster dynamic performance is attributed to the fact that the enhanced  $Li_2O$  matrix supplies a highly stable network around the Sn nanoparticles and provides a relatively good electrical contact.



**Figure 8.** Impedance spectra of the  $SnO_x$  films deposited at different Ar/ $O_2$  flow ratios: (a) 30/0, (b) 29/1, (c) 28/2, (d) 26/4, (e) 25/5, (f) 24/6 and (g) 23/7. The schematic diagram in (h) shows the equivalent circuit.

#### 4. Conclusions

The SnO<sub>x</sub> films with various oxygen deficiencies were deposited with different Ar/O<sub>2</sub> flow ratios using the pDC–RMS method. The main focus was on improving the cycle performance by selecting proper stoichiometry SnO<sub>x</sub>. First, the SnO<sub>x</sub> films were identified as a mixture of Sn, SnO and SnO<sub>2</sub> by comparing the Sn 3d and O 1s spectra using the deconvolution procedure. Second, all physical properties (transmittance, crystal structure, density and surface morphology) of the SnO<sub>x</sub> films showed a sudden transition at the deposition condition of Ar/O<sub>2</sub> = 26/4, consistent with the turning point for composition evolution. Third, the increase in oxidation degree within the SnO<sub>x</sub> films determined the reaction transition from “single alloying” to “conversion + alloying” mode. A certain amount of Li<sub>2</sub>O prevented the Li–Sn alloy from suffering mechanical deterioration during repeated discharge/charge cycles, and the SnO<sub>1.71</sub> film deposited with Ar/O<sub>2</sub> = 23/7 showed the highest reversible capacity of 396.1 mAh/g at the 50th cycle with a current density of 44 μA/cm<sup>2</sup>.

**Supplementary Materials:** The following are available online at <https://www.mdpi.com/article/10.3390/ma14071803/s1>. Figure S1: EDS of the Sn element distribution in as-grown SnO<sub>x</sub> films; Figure S2: SEM images and Sn, O elements distribution of the SnO<sub>x</sub> films after cycling; Figure S3: Cross-section SEM images and film thickness of the SnO<sub>x</sub> films; Figure S4: AFM images are supported to show the evolution of topography and surface roughness; Figure S5: XRR measurement principle and fitting model used to calculate the film density; Figure S6: the XPS survey spectra used to confirm the types of chemical composition; Figure S7: the initial discharge/charge curves as a supplementary content are used to exhibit the difference in electrochemical performance between different SnO<sub>x</sub> film electrodes; Figure S8: the comparison of specific XPS spectra after Ar<sup>+</sup> etching for the two films deposited with Ar/O<sub>2</sub> = 30/0 and Ar/O<sub>2</sub> = 23/7; Figure S9: the XPS spectra of the SnO<sub>2</sub> standard material.

**Author Contributions:** Y.M. and W.L. conceived the idea. Y.M., W.L., Y.W., J.L., X.Z. (Xiaofeng Zhang) and J.P. carried out material synthesis, characterization and electrochemical characterization. Y.M., W.L., X.Z. (Xuan Zhang), Z.F. and Y.Y. co-wrote the paper. All the authors discussed the results and commented on the manuscript. All authors have read and agreed to the published version of the manuscript.

**Funding:** This research was funded by The National Natural Science Foundation of China, grant number “21603204” and “51802297”.

**Institutional Review Board Statement:** Not applicable.

**Informed Consent Statement:** Not applicable.

**Data Availability Statement:** Data sharing not applicable.

**Acknowledgments:** The authors gratefully acknowledge the financial support of The National Natural Science Foundation of China (Grant No. 21603204, 51802297) and Beijing Institute of Aeronautical Materials.

**Conflicts of Interest:** The authors declare no conflict of interest.

#### References

1. Wang, D.; Zhou, J.S.; Li, Z.P.; Li, J.K.; Hou, L.; Gao, F.M. Uniformly expanded interlayer distance to enhance the rate performance of soft carbon for lithium-ion batteries. *Ionics* **2019**, *25*, 1531–1539. [[CrossRef](#)]
2. Lee, B.S. A review of recent advancements in electrospun anode materials to improve rechargeable lithium battery performance. *Polymers* **2020**, *12*, 2035. [[CrossRef](#)] [[PubMed](#)]
3. Florian, Z.; Daniel, B.; Thomas, B.; Dina, F.I. Tin oxide-based nanomaterials and their application as anodes in lithium-ion batteries and beyond. *ChemSusChem* **2019**, *12*, 4240–4259.
4. Vaughey, J.T.; Ohara, J.; Thackeray, M.M. Intermetallic insertion electrodes with a zinc blend e-type structure for Li batteries: A study of Li<sub>x</sub>InSb (0 ≤ x ≤ 3). *Electrochem. Solid-State Lett.* **2000**, *3*, 13–17. [[CrossRef](#)]
5. Wachtler, M.; Besenhard, J.O.; Winter, M. Tin and tin-based intermetallics as new anode materials for lithium-ion cells. *J. Power Sources* **2001**, *94*, 189–193. [[CrossRef](#)]

6. Ferraresi, G.; Villevieille, C.; Czekaj, I.; Horisberger, H.; Novak, P.; Kazzi, M.E. SnO<sub>2</sub> model electrode cycled in Li-ion battery reveals the formation of Li<sub>2</sub>SnO<sub>3</sub> and Li<sub>8</sub>SnO<sub>6</sub> phases through conversion reactions. *ACS Appl. Mater. Interfaces* **2018**, *10*, 8712–8720. [[CrossRef](#)] [[PubMed](#)]
7. Hung, J.Y.; Zhong, L.; Wang, C.M.; Sullivan, J.P.; Xu, W.; Zhang, L.Q.; Mao, S.X.; Hudak, N.S.; Liu, X.H.; Subramanian, A.; et al. In situ observation of the electrochemical lithiation of a single SnO<sub>2</sub> nanowire electrode. *Science* **2010**, *330*, 1515–1520. [[CrossRef](#)] [[PubMed](#)]
8. Zhang, G.M.; Wang, T.; Cao, G. Promises and challenges of tin-based compounds as anode materials for lithium-ion batteries. *Int. Mater. Rev.* **2015**, *60*, 330–352. [[CrossRef](#)]
9. Etacheri, V.; Gulain, A.S.; Caruthers, S.J.; Daniel, G.; Nedelec, J.M.; Kessler, V.G.; Pol, V.G. Ordered network of interconnected SnO<sub>2</sub> nanoparticles for excellent lithium-ion storage. *Adv. Energy Mater.* **2014**, *5*, 1401289. [[CrossRef](#)]
10. Kong, X.H.; Yu, D.P.; Li, Y.D. Synthesis of SnO<sub>2</sub> nanoribbons by direct oxidation of tin powders. *Chem. Lett.* **2003**, *32*, 100–101. [[CrossRef](#)]
11. Lu, Y.; Yanilmaz, M.; Chen, C.; Dirican, M.; Ge, Y.Q.; Zhu, J.D.; Zhang, X.W. Centrifugally spun SnO<sub>2</sub> microfibers composed of interconnected nanoparticles as the anode in sodium-ion batteries. *ChemElectroChem* **2015**, *2*, 1947–1956. [[CrossRef](#)]
12. Lakhdari, D.; Boulegane, A.; Belfenache, D.; Dehdouh, H. Electrochemical, structural and optical properties of SnO<sub>2</sub> thin films. *CIER-PET* **2017**, *28*, 65–69.
13. Xie, M.; Sun, X.; George, S.M.; Zhou, C.G.; Lian, J.; Zhou, Y. Amorphous ultrathin SnO<sub>2</sub> films by atomic layer deposition on graphene network as highly stable anodes for lithium ion batteries. *ACS Appl. Mater. Inter.* **2015**, *7*, 27735–27742. [[CrossRef](#)]
14. Lee, W.H.; Son, H.C.; Moon, H.S.; Kim, Y.I.; Sung, S.H.; Kim, J.Y.; Lee, J.G.; Park, J.W. Stoichiometry dependence of electrochemical performance of thin film SnO<sub>x</sub> microbattery anodes deposited by radio frequency magnetron sputtering. *J. Power Sources* **2000**, *89*, 102–105. [[CrossRef](#)]
15. Park, M.G.; Lee, D.H.; Jung, H.; Choi, J.H.; Park, C.M. Sn-based nanocomposite for Li-ion battery anode with high energy density, rate capability, and reversibility. *ACS Nano* **2018**, *12*, 2955–2967. [[CrossRef](#)] [[PubMed](#)]
16. Djerdj, I.; Gracin, N.D.; Juraic, K.; Meljanac, D.; Radovic, I.B.; Pletikapic, G. Structural analysis of monolayered and bilayered SnO<sub>2</sub> thin films. *Surf. Coat. Technol.* **2012**, *211*, 24–28. [[CrossRef](#)]
17. Park, G.S.; Yang, G.M. Characterization of SnO<sub>2</sub> films on glass by transmission electron microscopy. *Thin Solid Films* **2000**, *365*, 7–11. [[CrossRef](#)]
18. Khan, A.F.; Mehmood, M.; Rana, A.M.; Bhatti, M.T. Effect of annealing on electrical resistivity of rf-magnetron sputtered nanostructured SnO<sub>2</sub> thin films. *Appl. Surf. Sci.* **2009**, *255*, 8562–8565. [[CrossRef](#)]
19. Batzill, M.; Burst, J.M.; Diebold, U. Pure and cobalt-doped SnO<sub>2</sub> (101) films grown by molecular beam epitaxy on Al<sub>2</sub>O<sub>3</sub>. *Thin Solid Films* **2005**, *484*, 132–139. [[CrossRef](#)]
20. Akgul, F.A.; Gumus, C.; Er, A.O.; Farha, A.H.; Akgul, G.; Ufuktepe, Y.; Liu, Z. Structural and electronic properties of SnO<sub>2</sub>. *J. Alloys Compd.* **2013**, *579*, 50–56. [[CrossRef](#)]
21. Zhao, L.Z.; Qiao, L.N.; Miao, H.; Su, S.H.; Ru, Q.; Hou, X.H. Influence of magnetron sputtering method on cyclic performance of tin film anodes. *Advan. Mater. Res.* **2012**, *51*, 1706–1709. [[CrossRef](#)]
22. Hou, X.H.; Hu, S.J.; Peng, W.; Zhang, Z.W.; Ru, Q. Study of lithium storage properties of the Sn-Ni alloys prepared by magnetic sputtering technology. *Acta Metall. Sin. (Engl. Lett.)* **2010**, *23*, 363–369.
23. Safi, I. Recent aspects concerning DC reactive magnetron sputtering of thin films: A review. *Surf. Coat. Technol.* **2000**, *127*, 203–218. [[CrossRef](#)]
24. Shanke, G.; Prathap, P.; Srivastha, K.M.K.; Singh, P. Effect of balanced and unbalanced magnetron sputtering processes on the properties of SnO<sub>2</sub> thin films. *Curr. Appl. Phys.* **2019**, *19*, 697–703. [[CrossRef](#)]
25. Mukhamedshina, D.M.; Bersenkanov, N.B.; Mit, K.A.; Valitova, I.; Botvin, V.A. Investigation of properties of thin oxide films SnO<sub>x</sub> annealed in various atmospheres. *Thin Solid Films* **2006**, *495*, 316–320. [[CrossRef](#)]
26. Boltz, J.; Koehl, D.; Wutting, M. Low temperature sputter deposition of SnO<sub>x</sub>:Sb films for transparent conducting oxide applications. *Surf. Coat. Technol.* **2010**, *205*, 2455–2460. [[CrossRef](#)]
27. Denarun, D.P.; Rajeeb, B.; Ghanashyam, K. Effects of metal doping on photoinduced hydrophilicity of SnO<sub>2</sub> thin films. *Bull. Mater. Sci.* **2015**, *38*, 1–6.
28. Ao, D.; Lchimura, M. Deposition and characterization of Sb and Cu doped nanocrystalline SnO<sub>2</sub> thin films fabricated by the photochemical method. *J. Non-Cryst. Solids* **2012**, *358*, 2470–2473. [[CrossRef](#)]
29. Wu, M.; Li, X.W.; Zhou, Q.; Ming, H.; Adkins, J.; Zheng, J.W. Fabrication of Sn film via magnetron sputtering towards understanding electrochemical behavior in lithium-ion battery application. *Electrochim. Acta* **2014**, *123*, 144–150. [[CrossRef](#)]
30. Read, J.; Foster, D.; Wolfensitnce, J.; Behl, W. SnO<sub>2</sub>-carbon composites for lithium-ion battery anodes. *J. Power Sources* **2001**, *96*, 277–281. [[CrossRef](#)]
31. Wang, H.; Wu, Y.M.; Bai, Y.S.; Zhou, W.; An, Y.R.; Li, J.H.; Guo, L. The self-assembly of porous microspheres of tin dioxide octahedral nanoparticles for high performance lithium ion battery anode materials. *J. Mater. Chem.* **2011**, *21*, 10189–10194. [[CrossRef](#)]
32. Tao, Y.; Zhu, B.L.; Yang, Y.T.; Wu, J.; Shi, X.W. The structural, electrical, and optical properties of SnO<sub>2</sub> films prepared by reactive magnetron sputtering: Influence of substrate temperature and O<sub>2</sub> flow rate. *Mater. Chem. Phys.* **2020**, *250*, 123129. [[CrossRef](#)]

33. Chen, Z.W.; Lai, J.K.L.; Shek, C.H. Insights into micro structural evolution from nanocrystalline SnO<sub>2</sub> thin films prepared by pulsed laser deposition. *Phys. Rev. B* **2004**, *70*, 165314. [[CrossRef](#)]
34. Korotcenkov, G.; Brinzari, V.; Boris, I. (Cu, Fe, Co, or Ni)-doped tin dioxide films deposited by spray pyrolysis: Doping influence on film morphology. *J. Mater. Sci.* **2008**, *43*, 2761–2770. [[CrossRef](#)]
35. Qiu, S.L.; Pmarcus, M. Equilibrium lines and barriers to phase transitions: The cubic diamond to beta-tin transition in Si from first principles. *J. Phys.-Condens. Mat.* **2012**, *24*, 225501. [[CrossRef](#)]
36. Huggins, R.A. Lithium alloy negative electrodes. *J. Power Sources* **1999**, *81–82*, 13–19. [[CrossRef](#)]
37. Joo, Y.H.; Wi, J.H.; Lee, W.J.; Chung, Y.D.; Cho, D.Y.; Kang, S.; Um, D.S.; Kim, C.I. Work function tuning of zinc-tin oxide thin films using high-density O<sub>2</sub> plasma treatment. *Coatings* **2020**, *10*, 1026. [[CrossRef](#)]
38. Alessandro, D.; Cinzia, C.; Monica, S.; Macis, S.; Bekec, B.; Fanetti, M.; Piseri, P.; Marcelli, A.; Coreno, M. Interplay among work function, electronic structure and stoichiometry in nanostructured VO<sub>x</sub> films. *Phys. Chem. Chem. Phys.* **2020**, *20*, 6282–6290.
39. Gao, Y.; Wang, Z.; Chen, L. Work function, a new viewpoint to understand the electrolyte/electrode interface reaction. *J. Mater. Chem. A* **2015**, *46*, 1–20.
40. Cherkashinin, G.; Hausbrand, R.; Jaegermann, W. Performance of Li-ion batteries: Contribution of electronic factors to the battery voltage. *J. Electrochem. Soc.* **2019**, *166*, A5308–A5312. [[CrossRef](#)]
41. Ane, E.; Stephan, L.K.; Oleksandr, B. Work function evolution in Li anode processing. *Adv. Energy Mater.* **2020**, *10*, 2000520.
42. Aravindana, V.; Jinesha, K.B.; Prabhakar, R.R.; Kale, V.S.; Madhavi, S. Atomic layer deposited (ALD) SnO<sub>2</sub> anodes with exceptional cyclability for Li-ion batteries. *Nano Energy* **2013**, *2*, 720–725. [[CrossRef](#)]
43. Weast, R.C. *Handbook of Chemistry and Physics*; CRC Press: Boca Raton, FL, USA, 1988.
44. Themlin, J.M.; Chataib, M.; Hennard, L.; Lambin, P.; Darville, J.; Gilles, J.M. Characterization of tin oxides by X-ray-photoemission spectroscopy. *Phys. Rev. B* **1992**, *46*, 2460–2467. [[CrossRef](#)]
45. Marichy, C.; Donato, N.; Willinger, M.G.; Latino, M.; Karpinsky, D.; Yu, S.H.; Neri, G.; Pima, N. Tin dioxide sensing layer grown on tubular nanostructures by a non-aqueous atomic layer deposition process. *Adv. Funct. Mater.* **2011**, *21*, 658–666. [[CrossRef](#)]
46. Kwoka, M.; Ottaviano, L.; Passacantando, M.; Santucci, S.; Czempic, G.; Szuber, J. XPS study of the surface chemistry of CVD SnO<sub>2</sub> thin films after oxidation. *Thin Solid Films* **2000**, *490*, 36–42. [[CrossRef](#)]
47. Asbury, D.A.; Hoflund, G.B. A surface study of the oxidation of polycrystalline tin. *J. Vac. Sci. Technol. A* **1987**, *5*, 1132–1135. [[CrossRef](#)]
48. Larciprete, R.; Borsella, E.; Padova, P.D.; Perfetti, P.; Faglia, G.; Sberveglieri, G. Organotin films deposited by laser-induced CVD as active layers in chemical gas sensors. *Thin Solid Films* **1998**, *323*, 291–295. [[CrossRef](#)]
49. Wang, S.R.; Huang, J.; Geng, L.; Zhu, B.L.; Wang, X.Y.; Wu, S.H.; Zhang, S.M.; Huang, W.P. Tin dioxide supported nanometric gold: Synthesis, characterization, and low temperature catalytic oxidation of CO. *Catal. Lett.* **2006**, *108*, 97–102. [[CrossRef](#)]
50. Zhao, Y.L.; Dong, G.F.; Duan, L.; Qiao, J.; Zhang, D.Q.; Wang, L.D.; Qiu, Y. Impacts of Sn precursors on solution-processed amorphous zinc-tin oxide films and their transistors. *RSC Adv.* **2012**, *2*, 5307–5313. [[CrossRef](#)]
51. Zhu, Z.; Ma, J.; Luan, C.; Mi, W.; Lv, Y. Epitaxial growth of SnO<sub>2</sub> films on 6H-SiC (0 0 0 1) by MOCVD. *Mater. Res. Bull.* **2012**, *47*, 253–256. [[CrossRef](#)]
52. Oswald, S.; Hoffmann, M.; Zier, M. Peak position differences observed during XPS sputter depth profiling of the SEI on lithiated and delithiated carbon-based anode material for Li-ion batteries. *Appl. Surf. Sci.* **2017**, *401*, 408–413. [[CrossRef](#)]
53. Maibach, J.; Lindgren, F.; Eriklsson, H.; Edstrom, K.; Hahllin, M. Electric potential gradient at the buried interface between lithium-ion battery electrodes and the SEI observed using photoelectron spectroscopy. *J. Phys. Chem. Lett.* **2016**, *7*, 1775–1780. [[CrossRef](#)]
54. Zhao, S.; Xu, K.W. Impact of partial oxygen pressure on transmittance of RF reactively sputtered ZrO<sub>2</sub> films. *Funct. Mater. Lett.* **2004**, *35*, 3162–3164.
55. Chattaraj, P.K.; Maiti, B. Regioselectivity in the chemical reactions between molecules and protons: A quantum fluid density functional study. *J. Phys. Chem. B* **2004**, *108*, 658–664. [[CrossRef](#)]
56. Padova, P.D.; Larciprete, R.; Ottaviani, C.; Quaresima, C.; Perfetti, P.; Borsella, E.; Astaldi, C.; Comicioli, C.; Crotti, C.; Matteucci, M.; et al. Synchrotron radiation photoelectron spectroscopy of the O(2s) core level as a tool for monitoring the reducing effects of ion bombardment on SnO<sub>2</sub> thin films. *Appl. Surf. Sci.* **1996**, *104–105*, 349–353. [[CrossRef](#)]
57. Themlin, J.M.; Sporcken, R.; Darcille, J.; Gaudano, R.; Gilles, J.M.; Johnson, R.L. Resonant-photoemission study of SnO<sub>2</sub>: Cationic origin of the defect band-gap states. *Phys. Rev. B* **1990**, *42*, 11914–11926. [[CrossRef](#)]
58. Fang, C.S.; Pan, F.M.; Tse, W.S.; Honrng, S.R. Photoemission studies of ion bombardment effect on SnO<sub>2</sub> surfaces. *Surf. Sci.* **1989**, *211–212*, 279–288. [[CrossRef](#)]
59. Larciprete, R.; Borsella, E. Synchrotron radiation photoemission analysis of ArF laser deposited tin oxide. *J. Vac. Sci. Technol. A* **1993**, *11*, 336–341. [[CrossRef](#)]
60. Adrian, A.C.B.; Victor, M.P.; Wilfredo, O. Reactive sputtered ZnO thin films: Influence of the O<sub>2</sub>/Ar flow ratio on the oxygen vacancies and paramagnetic active sites. *Thin Solid Films* **2019**, *692*, 137641.
61. He, Z.B.; Wu, W.D.; Xu, H.; Zhang, J.C.; Tang, Y.J. The effects of O<sub>2</sub>/Ar flow ratio on the structure and properties of hafnium dioxide (HfO<sub>2</sub>) films. *Vacuum* **2006**, *81*, 211–214. [[CrossRef](#)]
62. Kwoka, M.; Krzywiecki, M. Rheotaxial growth and vacuum oxidation—Novel technique of tin oxide deposition—In situ monitoring of oxidation process. *Mater. Lett.* **2015**, *154*, 1–4. [[CrossRef](#)]

63. Tavassol, H.; Cason, M.W.; Nuzzo, R.G.; Gewirth, A.A. Influence of oxides on the stress evolution and reversibility during SnO<sub>x</sub> conversion and Li–Sn alloying reactions. *Adv. Energy Mater.* **2014**, *1400317*, 1–10.
64. Zuo, T.T.; Wu, X.W.; Yang, C.P.; Yin, Y.X.; Ye, H.; Li, N.W.; Guo, Y.G. Graphitized carbon fibers as multifunctional 3D current collectors for high areal capacity Li anodes. *Adv. Mater.* **2017**, *29*, 1700389. [[CrossRef](#)] [[PubMed](#)]
65. Mohamedi, M.; Lee, S.J.; Takahashi, D.; Itoh, T.; Uchida, I. Amorphous tin oxide films: Preparation and characterization as an anode active material for lithium ion batteries. *Electrochim. Acta* **2001**, *46*, 1161–1168. [[CrossRef](#)]
66. Belliard, F.; Connor, P.A.; Ircine, J.T.S. Novel tin oxide–based anodes for Li–ion batteries. *Solid State Ion.* **2000**, *135*, 163–167. [[CrossRef](#)]
67. Aracindan, V.; Gnanaraj, J.; Madhaci, S.; Liu, H.K. Lithium–ion conducting electrolyte salts for lithium batteries. *Chem. A Eur. J.* **2011**, *17*, 14326–14346. [[CrossRef](#)] [[PubMed](#)]
68. Inaba, M.; Uno, T.; Tasaka, A. Irreversible capacity of electrodeposited Sn thin film anode. *J. Power Sources* **2015**, *146*, 473–477. [[CrossRef](#)]
69. Courtney, I.A.; Mckinnon, W.R.; Dahn, J.R. On the aggregation of tin in SnO composite glasses caused by the reversible reaction with lithium. *J. Electrochem. Soc.* **1999**, *146*, 59–68. [[CrossRef](#)]
70. Menkin, S.; Golodnitsky, D.; Peled, E. Artificial solid–electrolyte interphase (SEI) for improved cyclability and safety of lithium–ion cells for EV applications. *Electrochem. Commun.* **2009**, *11*, 1789–1791. [[CrossRef](#)]
71. Chiu, K.F.; Lin, H.C.; Lin, K.M.; Lin, T.Y.; Shieh, D.T. Anode–shielded, sputter–deposited nanocrystalline Sn thin–film anodes for lithium–ion batteries. *J. Electrochem. Soc.* **2006**, *153*, A920–A924. [[CrossRef](#)]
72. Wu, H.; Chan, G.; Choi, J.W.; Ryu, I.; Yao, Y.; Mcdowell, M.T.; Lee, S.W.; Jackson, A.; Yang, Y.; Hu, L.B.; et al. Stable cycling of double–walled silicon nanotube battery anodes through solid–electrolyte interphase control. *Nat. Nanotechnol.* **2012**, *7*, 310–315. [[CrossRef](#)] [[PubMed](#)]
73. Todd, A.D.W.; Ferguson, P.P.; Fleischauer, M.D.; Dahn, J.R. Tin–based materials as negative electrodes for Li–ion batteries: Combinatorial approaches and mechanical methods. *Int. J. Energy Res.* **2010**, *4*, 535–555. [[CrossRef](#)]
74. Knoops, H.C.M.; Donders, M.E.; Kesseks, W.M.M.; Sanden, M.C.M.; Notten, P.H. Atomic layer deposition for nanostructured Li–ion batteries. *J. Vac. Sci. Technol. A* **2012**, *30*, 010801. [[CrossRef](#)]
75. Bard, A.J.; Faulkner, L.R. *Electrochemical Methods: Fundamentals and Applications*; Wiley: New York, NY, USA, 1980; Volume 2.
76. Santos, P.J.; Brousse, T.; Sanchez, L.; Morales, J.; Schleich, D.M. Antimony doping effect on the electrochemical behavior of SnO<sub>2</sub> thin film electrode. *J. Power Sources* **2001**, *97–98*, 232–234. [[CrossRef](#)]